Point2Building: Reconstructing Buildings from Airborne LiDAR Point Clouds

Yujia Liu^a, Anton Obukhov^a, Jan Dirk Wegner^b, Konrad Schindler^{a,*}

^aPhotogrammetry and Remote Sensing, ETH Zürich, 8093 Zürich, Switzerland ^bDepartment of Mathematical Modeling and Machine Learning, University of Zürich, 8057 Zürich, Switzerland

Abstract

We present a learning-based approach to reconstruct buildings as 3D polygonal meshes from airborne LiDAR point clouds. What makes 3D building reconstruction from airborne LiDAR hard is the large diversity of building designs and especially roof shapes, the low and varying point density across the scene, and the often incomplete coverage of building facades due to occlusions by vegetation or to the viewing angle of the sensor. To cope with the diversity of shapes and inhomogeneous and incomplete object coverage, we introduce a generative model that directly predicts 3D polygonal meshes from input point clouds. Our autoregressive model, called Point2Building, iteratively builds up the mesh by generating sequences of vertices and faces. This approach enables our model to adapt flexibly to diverse geometries and building structures. Unlike many existing methods that rely heavily on pre-processing steps like exhaustive plane detection, our model learns directly from the point cloud data, thereby reducing error propagation and increasing the fidelity of the reconstruction. We experimentally validate our method on a collection of airborne LiDAR data of Zurich, Berlin and Tallinn. Our method shows good generalization to diverse urban styles.

Keywords: Airborne LiDAR Point Clouds, Deep Learning, Building Reconstruction, Autoregressive Generative Models, Transformers

1. Introduction

The conversion of urban environments into digital representations is important across remote sensing, computer vision, computer graphics, and photogrammetry. Three-dimensional models of urban structures offer broad utility in applications such as visualization, navigation, and

Email address: schindler@ethz.ch (Konrad Schindler)

^{*}Corresponding Author.

urban planning (Poullis and You, 2009; Lafarge and Mallet, 2012; Cheng et al., 2011). Among sensing technologies for urban modeling, airborne Light Detection and Ranging (LiDAR) (Liu, 2008; Chen, 2007; Li et al., 2020; Sampath and Shan, 2007) has become particularly important. Although point clouds from LiDAR are just one of many data sources for 3D modeling, their ability to accurately capture large-scale geometry is particularly promising for cityscale perception of urban environments. Various formats were developed to represent 3D surfaces. Examples include NURBS for smooth, accurate surfaces, voxel grids for volumetric analysis, subdivision surfaces for computer graphics and animation, and implicit surfaces for mathematical descriptions or scientific visualizations. Converting point clouds to such explicit or implicit representations involves diverse methods, from traditional geometry-based techniques (Hoppe et al., 1992; Kazhdan et al., 2006; Boissonnat and Oudot, 2005) to learningbased approaches (Groueix et al., 2018; Guerrero et al., 2018; Park et al., 2019). Methods for explicit surfaces utilize meshes (Gupta, 2020; Jiang et al., 2020, 2019) or patches (Badki et al., 2020; Groueix et al., 2018; Ma et al., 2021) to directly define geometry, known for their efficiency. Implicit methods represent shapes with functions over voxel grids (Dai et al., 2018; Jiang et al., 2017; Liao et al., 2018) or neural networks (Chen and Zhang, 2019; Mescheder et al., 2019; Park et al., 2019; Liu et al., 2023), offering a high level of visual detail and compelling view synthesis (Martin-Brualla et al., 2021; Mildenhall et al., 2021), but at a higher computational cost.

Among these surface representations, we focus on 3D polygonal meshes for representing buildings. Polygonal meshes (Botsch et al., 2010; Chen et al., 2020; Nan and Wonka, 2017) are an effective representation format comprising interconnected vertices and faces. It provides compact structural information beyond dense triangulations (Fabio et al., 2003; Salman et al., 2010) and thus appears an apt choice for the 3D representation of urban areas.

Traditional approaches to 3D polygon reconstruction (Halla, 1999; Verma et al., 2006) have relied om learning-free algorithms that are often rigid and have limited adaptability. Furthermore, a few existing learning-based methods (Chen et al., 2022, 2023) often suffer from a lack of flexibility, being tied down by the constraints of their initial processing stages, like primitive segmentation (Liu et al., 2023) or planar segment detection (Yang et al., 2010) with methods like RANSAC (Schnabel et al., 2007; Li and Shan, 2022). Such steps can propagate errors, leading to inaccuracies in the final model due to incorrect decisions in earlier steps.

Building upon these insights, we aim to employ a more integrated learning-based approach, one that avoids the dependency on initial segmentation or plane detection and reduces the risk of error accumulation.

To this end, we adopt an autoregressive generative model, PolyGen (Nash et al., 2020), to reconstruct polygonal buildings from 3D LiDAR point clouds. PolyGen is especially well-suited for our needs because it naturally handles the diversity in building topology without relying on pre-segmentation or prior primitive fitting. It brings the advantage of learning directly from data, allowing for a more effective and adaptive representation of architectural features than existing methods reliant on hand-designed geometric descriptors. PolyGen operates in two stages. First, it produces the positions of vertices based on the input 3D point cloud data, effectively capturing the spatial configuration of the target structures. Second, it constructs the mesh faces that connect the created vertices, forming the object surface.

The autoregressive nature of PolyGen's generative process is affected by common issues shared by most modern generative models (e.g., hallucinations). We turn the built-in diversity of the generated output into an advantage by sampling multiple reconstructions conditioned on the same input point cloud, and keeping only the one that best satisfies a set of plausibility checks.

We have conducted experiments on a combined dataset encompassing aerial LiDAR scans sourced from the Federal Office of Topography (swisstopo, 2023) and corresponding 3D polygonal mesh models provided by the City of Zurich (Stadt Zurich, 2023). Our method trained on this dataset shows improvements compared to existing approaches across a range of evaluation metrics. Additionally, to demonstrate the method's adaptability and effectiveness, we include experiments on further datasets from Berlin and Tallinn in our evaluation.

2. Related Work

Reconstructing buildings from point cloud data (Brenner et al., 2001) involves specialized techniques that address the regular and deliberate design typical of architectural structures. These methods are developed to accurately represent essential architectural features such as flat surfaces, sharp edges, and key elements like floorplans, facades, and outer walls. They must also be flexible enough to handle buildings of various sizes and complexities, from small single-family homes to large commercial complexes. In reviewing the field of building geometry

reconstruction, our focus is primarily on the generation of building models in the polygonal representation. The methods in this area can be broadly categorized into model-based, graph-based, and space-partitioning-based approaches.

2.1. Model-based approaches

Model-based (a.k.a. template-based) methods are a common strategy in 3D building reconstruction from point clouds. These methods operate under the assumption that the complex architecture of buildings can be approximated using a library of geometric standard shapes. In urban architecture, building roofs have received most attention. Roofs are modeled as combinations of predefined shapes (Kada and McKinley, 2009; Huang et al., 2013) like a saddleback, pent, flat, tent, mansard, etc. These methods typically start with extracting and refining the outlines of building footprints. The refined footprints are segmented into distinct 2D sections. The segmentation subdivides the reconstruction task into smaller subtasks that each identifying a roof style and fit the corresponding model parameters, steps for which established methods are available. For example, Poullis et al. (2008) use Gaussian mixture models to determine the parameters of basic shapes. Kada and McKinley (2009) rely on the orientation of roof surfaces to classify roof types and employ specific height measurements for parameter estimation. Techniques like the reversible jump Markov Chain Monte Carlo model (Huang et al., 2013) have also been utilized to fit these parameters to the input data. While modelbased methods have provided a solid framework for reconstructing 3D buildings, they are often bounded by their inherent assumptions, especially the selected collection of templates, which may not be able to cover the full architectural diversity. Recent advances in urban modeling have increasingly been driven by techniques that offer greater flexibility and can move beyond the constraints of predefined template shapes.

2.2. Graph-based approaches

Various graph-based methods have also been investigated (Chen and Chen, 2008; Schindler et al., 2011; Van Kreveld et al., 2011; Sampath and Shan, 2009). They generally focus on extracting geometric primitives, which are then linked into a graph that captures the adjacency relations. By intersecting these planar primitives, edges are reconstructed, forming a building model (Dorninger and Pfeifer, 2008; Maas and Vosselman, 1999; Vosselman et al., 2001). Challenges emerge when missing or spurious connections between primitives disrupt the graph's

connectivity, degrading the reconstruction quality. To address these difficulties, a hybrid approach (Lafarge and Alliez, 2013; Labatut et al., 2009) was introduced that combines two distinct elements: it uses polyhedral shapes to mark regions with high confidence levels and dense triangle meshes to represent areas of greater complexity accurately. Thus, it balances precision and the ability to handle complex structures. Another method (Zhou and Neumann, 2010, 2011), 2.5D dual contouring. It starts by projecting the point cloud data into a two-dimensional grid. Next, it finds so-called hyper-points within this grid, i.e., sets of 3D points having the same x-y coordinates yet different z values. These are then connected to form a graph, which is optimized by collapsing subtrees and merging similar branches to reduce complexity. Finally, a seamless mesh is generated by connecting the hyper-points into a watertight model.

Graph-based methods share the advantage that they are not confined to a predetermined set of geometric primitives, allowing for the reconstruction of various building structures. Nonetheless, these techniques may encounter issues related to topological correctness and can be computationally demanding.

2.3. Space-Partition-based approaches

Another class of building reconstruction methods involves dividing the volume containing the input point cloud into a redundant set of elementary shapes, which are then pruned to form an approximate model of the building. For example, Verdie et al. (2015) break down the space around the building into polyhedral cells, which are then evaluated by a Min-Cut formulation to determine whether they fall within the building polyhedra. PolyFit (Nan and Wonka, 2017) generates a collection of potential faces by the intersecting planes identified with RANSAC. Selecting the faces that most accurately represent the building's surface is approached as a binary integer linear program, with a strict constraint of edge-face connections. PolyFit is computationally intensive, particularly when handling complex structures that yield many potential faces to be considered.

Upon review, it becomes evident that each 3D reconstruction approach has different advantages and limitations. Model-based methods are structured and efficient, suitable for quick reconstruction tasks. However, they often depend on a finite set of predefined shapes, which may limit their applicability to diverse architectural styles. Graph-based strategies offer greater flexibility and adaptability to handle complex structures yet tend to be prone to connectivity errors affecting the reconstructed models' integrity. Conversely, space-

partition-based techniques provide a detailed decomposition of 3D space but face challenges in computational efficiency, particularly when dealing with large-scale structures.

3. Method

We use an autoregressive model to sequentially predict mesh elements, conditioned on the input point cloud. This method is distinct from conventional 3D reconstruction techniques in that it relies on a sequential, generative process rather than discriminative classification or regression of shape primitives (respectively, graphs). It is inspired by and adapted from PolyGen (Nash et al., 2020), which pioneered the use of autoregressive transformer models (Vaswani et al., 2017) for 3D mesh generation.

The method consists of two main modules, as shown in Fig. 1: the vertex module, which comprises a point cloud feature extractor and a block for vertex generation, and the face module. The vertex module operates by predicting the positions of vertices conditioned on point cloud features, effectively learning the underlying geometric structure of the shapes it is trained on. After vertex prediction, the face module sequentially generates mesh faces that connect the vertices to form the object surface. Each generated mesh is evaluated against predefined plausibility rules, ensuring that the final model adheres to minimal criteria for a valid building model. The process is repeated until the mesh meets all required criteria.

3.1. Vertex Module

The vertex module integrates a point cloud feature extractor with a transformer-based decoder, and generates a joint probability distribution for a sequence of vertices, as depicted in Fig. 2.

3.1.1. Sparse 3D CNN for Feature Extraction

The input point cloud (normalized to fit within a unit sphere) is encoded using a sparse convolutional neural network (SparseCNN), as implemented in the Minkowski Engine (Choy et al., 2019). This network takes a set of 3D points, denoted as \mathcal{P} , and outputs a set of context embeddings (Guo et al., 2022).

Initially, these points are discretized using a grid with a resolution of $128 \times 128 \times 128$. Subsequent stages involve convolutional operations paired with pooling to gradually reduce the

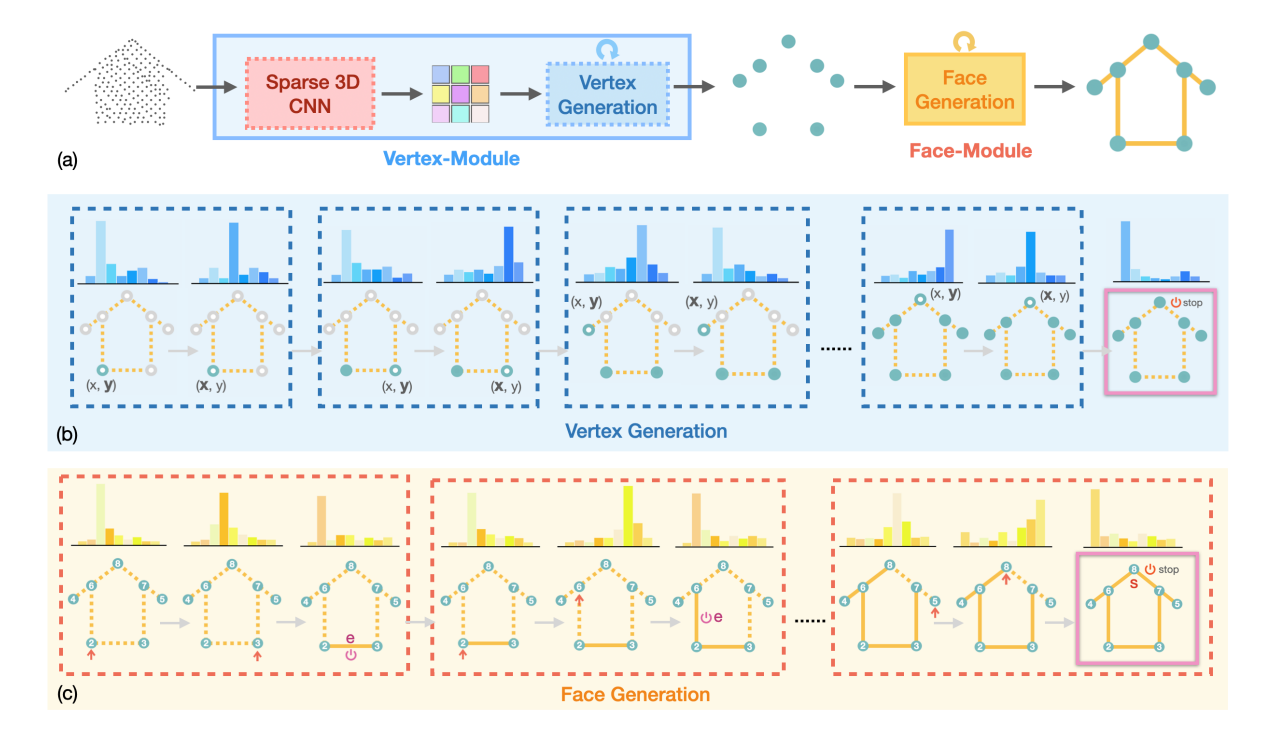


Figure 1: (a) Overview of the proposed pipeline visualized with cartoon 2D data. The actual implementation operates in 3D. (b) Stages of processing the cartoon 2D data. Each stage generates tuples of coordinates of one vertex. In the given 2D case, (y, x) tuples are generated. For real data, we generate (z, y, x) tuples. (c) Stages of assembling vertices into surfaces. At each stage, only one surface primitive corresponding to one line segment in the visualized cartoon 2D case) or a polyline capturing a polygon on a single plane (in the real 3D case) is created.

spatial resolution of the data to a $16 \times 16 \times 16$ grid, stored in the form of grid indices and feature vectors.

3.1.2. Block for Vertex Generation

The second block learns to produce vertex sequences conditioned on voxelized features extracted in the previous step.

Quantization-Driven Vertex Modeling. The vertices of a mesh are treated as discrete units through quantization. By implementing an 8-bit uniform quantization within the bounding box of the point cloud, we compress the point cloud information, merging vertices that are close to each other, akin to how SparseCNN discretizes space into a grid. We model the vertices using a categorical distribution along each axis. The generative phase of our model outputs logits that align with this distribution. The usage of quantization is similar to that applied by van den Oord et al. (2016a,b), leveraging a categorical distribution for its flexibility in modeling various

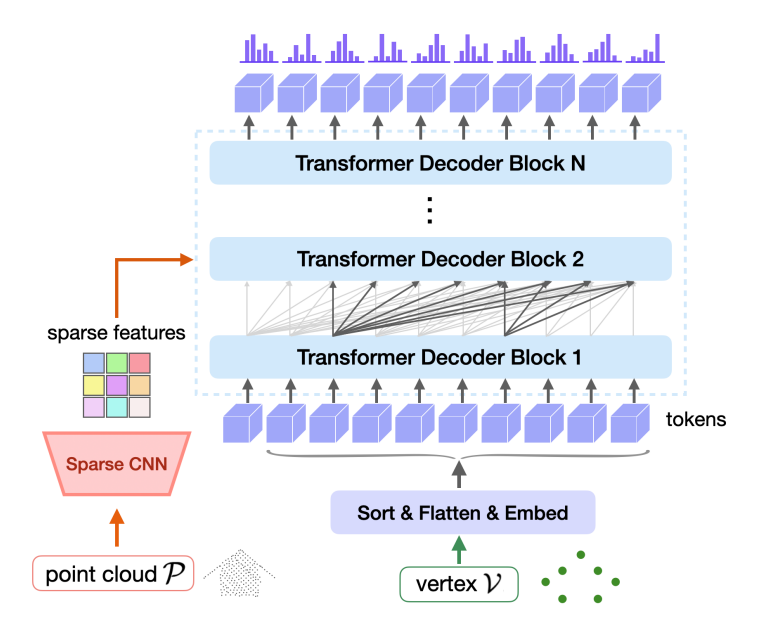


Figure 2: Illustration of vertex module architecture, comprising a point cloud encoder and a transformer-based decoder. Initially, the input point cloud is processed through SparseCNN, resulting in a sequence of context embeddings. The transformer decoder then applies cross-attention to these embeddings following a self-attention layer, analogous to the mechanism in the original machine translation Transformer model. Vertices are ordered according to their z, y, and x coordinates, converted into a flat sequence, and subsequently transformed into tokens as detailed in Section 3.1.2. For each token, the module predicts a distribution for the subsequent vertex coordinate value.

distributions without making assumptions about their shape.

Vertex Sequence Modeling. At each step, the vertex module outputs a probability distribution over vertex coordinates, conditioned on previously predicted vertex coordinates and input features. Sequence element order and other sequence formation conventions are an important part of any autoregressive framework. Therefore, ground truth vertex coordinate tuples (x, y, z) are reversed and sorted lexicographically to establish a reliable vertex order from bottom to top, left to right, and far to near. Subsequently, the list of sorted tuples are flattened into a raw sequence of tokens $(z_0, y_0, x_0, z_1, y_1, x_1, z_2, y_2, x_2, \cdots)$, terminated by a stopping token s as shown in Fig. 3.

Vertex Embedding. Each input token (quantized vertex coordinate) is encoded with three distinct embeddings: the coordinate embedding, which classifies the token as a spatial coordinate (x, y or z); the position embedding, which identifies the token's sequential order within the vertex sequence; and the value embedding, which conveys the quantized numerical value of the token's coordinate. The process is demonstrated in Fig. 4.

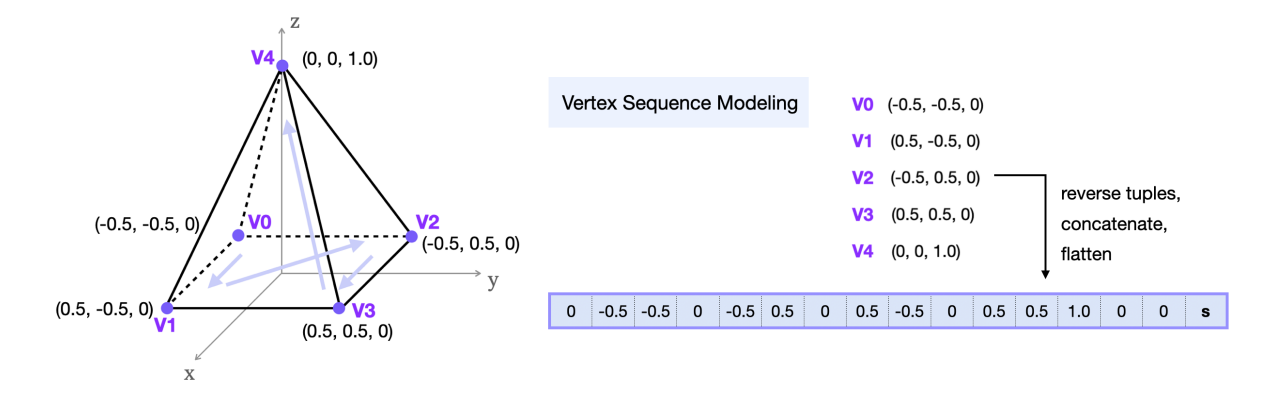


Figure 3: Illustration of creating ordered vertex sequence. The order is established by sorting according to zcoordinates, the vertical dimension. If z match, sorting proceeds by y, then by x to avoid ambiguities. A stopping
token s is added to signify the conclusion of the flattened vertex sequence.

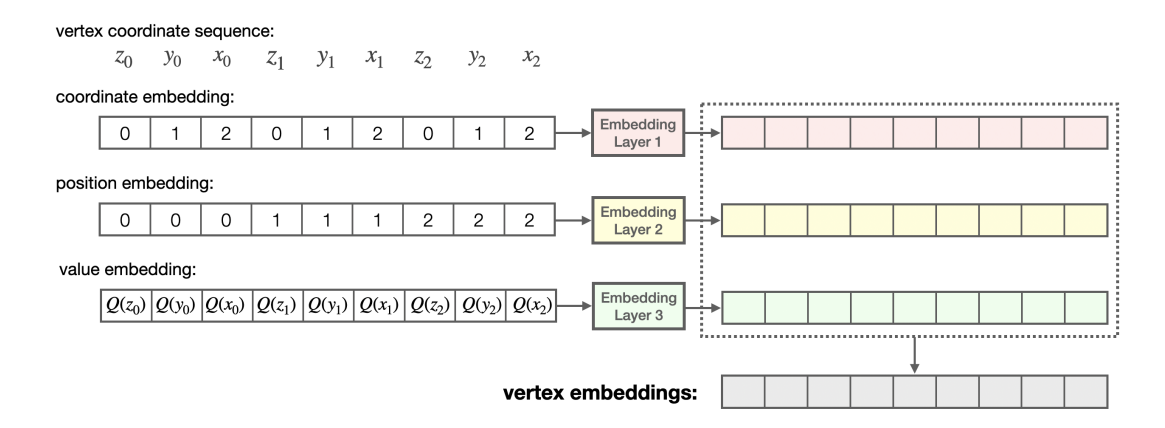


Figure 4: Illustration of vertex embedding process. x, y, and z are coordinates of vertices. $Q(\cdot)$ is the simple quantization function. For each token, the result vertex embeddings are obtained by summing three distinct learned embeddings: the coordinate embedding, the position embedding, and the value embedding. Specifically, the value embedding layer (Embedding Layer 3) is configured to support a total of 257 unique embeddings, reflecting 256 possible coordinate values plus one additional embedding for the end of a sequence. Each of these embeddings is represented by a vector of 256 dimensions. The coordinate embedding layer (Embedding Layer 1), provides 3 unique embeddings corresponding to the x, y, and z coordinates, while the position embedding layer (Embedding Layer 2) accommodates embeddings for up to a maximum number of vertices +1, each reflecting a distinct position in the sequence.

Vertex Decoder. The vertex model employs the Transformer-based decoder introduced by Vaswani et al. (2017). It outputs a joint probability distribution over sequences of vertices. This is achieved by modeling it as a product of conditional distributions, where the likelihood of each vertex coordinate v_n depends on the previous vertex coordinates in the sequence.

$$p(V_{\text{seq}}; \theta) = \prod_{n=1}^{N_v} p(v_n | v_{< n}; \theta)$$

An autoregressive network is used as the backbone for the practical modeling of this distribution in a factorized manner. The model is trained to maximize the likelihood of sampled sequences under the model parameters θ and input conditions \mathcal{P} .

3.2. Face module

The Face module architecture employs a transformer-based encoder and decoder, detailed in Fig. 5. It learns to produce a sequence of faces conditioned on the vertices generated by the Vertex Module.

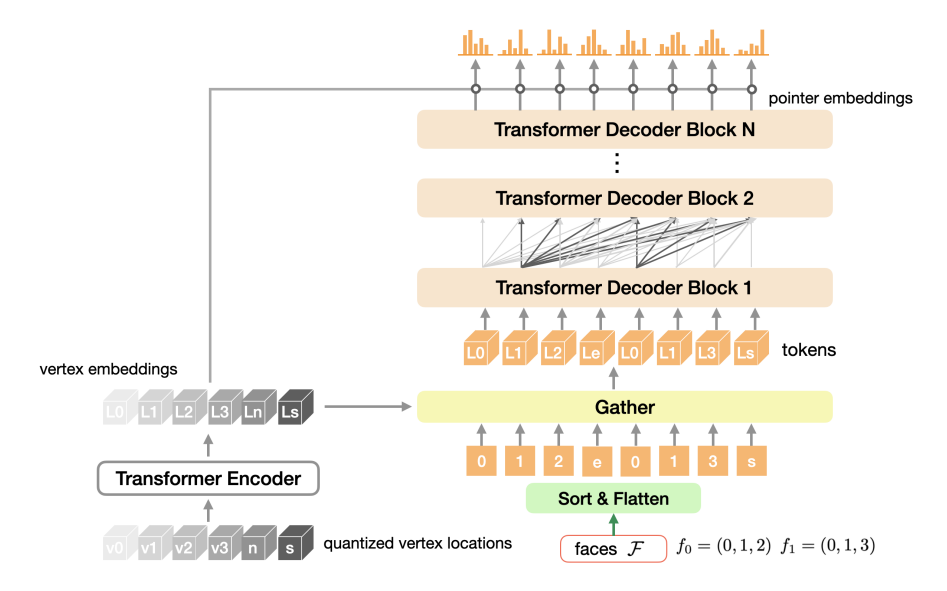


Figure 5: Illustration of the face module architecture, featuring a transformer-based encoder and decoder. The process begins with the transformation of quantized vertex locations by integrating embeddings across the three dimensions (x, y, z), akin to the 'value embedding' phase in Fig. 7. These transformed vertex embeddings are further refined by a transformer encoder. For the sorted, flattened faces, a 'gather' operation collects the corresponding embeddings for each vertex index within the faces. These collected embeddings, along with face-id and relative-position embeddings, constitute the face embeddings, as detailed in Fig. 7. They are then processed by a Transformer decoder, which predicts distributions over vertex indices at each decoding step, as well as the next-face token and the stopping token. The Transformer's final output layer generates pointer embeddings. These are compared against the vertex embeddings through a dot-product operation, yielding the final distributions over vertices.

Face Sequence Modeling. To structure the mesh faces, we sort them based on vertex indices. This sorting adheres to a simple rule: vertex indices within each face tuple do not decrease.

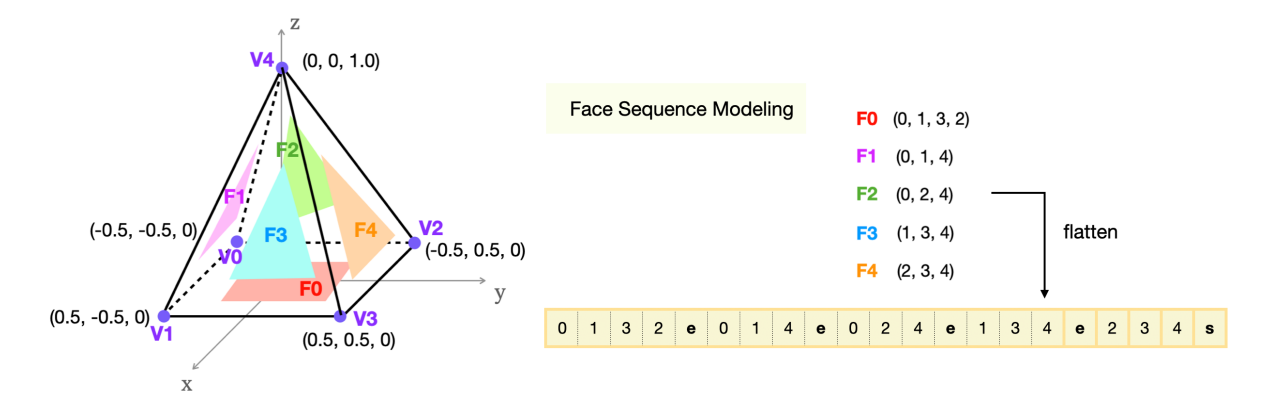


Figure 6: Illustration of creating ordered face sequence. Sorting bgins by identifying the smallest vertex index in each face. In situations with identical smallest indices, sorting proceeds by comparing subsequent lower indices within those faces. Vertices in each face are then reordered, starting with the lowest index, and an 'end-face' token e is added to denote the end of each vertex list. The sequence concludes with a stopping token s.

On the sequence level, face tuples are sorted lexicographically. To flatten the list of sorted face tuples, we introduce an 'end-face' token e as a delimiter between subsequent tuples. As for the vertex sequences, we terminate the concatenated sequence of tokens with a stopping token s, as shown in Fig. 6.

Face Embeddings. Similarly to the vertex model, we employ learned embeddings to represent both the position and the value associated with each token in the face module. The position of a token is characterized by two aspects: the specific face of the mesh to which it is assigned and its relative position within that face. For the value associated with each token, we assign vertex embeddings generated by a transformer encoder. This embedding process is demonstrated in Fig. 7.

Face Decoder. To address the variability in the size of vertex sets across different models, we adopt a strategy akin to the pointer network framework (Vinyals et al., 2015), as employed in PolyGen. This framework starts by encoding the vertex set and then uses an autoregressive network to generate a pointer vector at each step. This pointer vector is compared against the encoded vertex set through a dot-product operation, and the resulting values are then converted into a probability distribution over the vertices by applying the *softmax* function, forming the next face of the mesh.

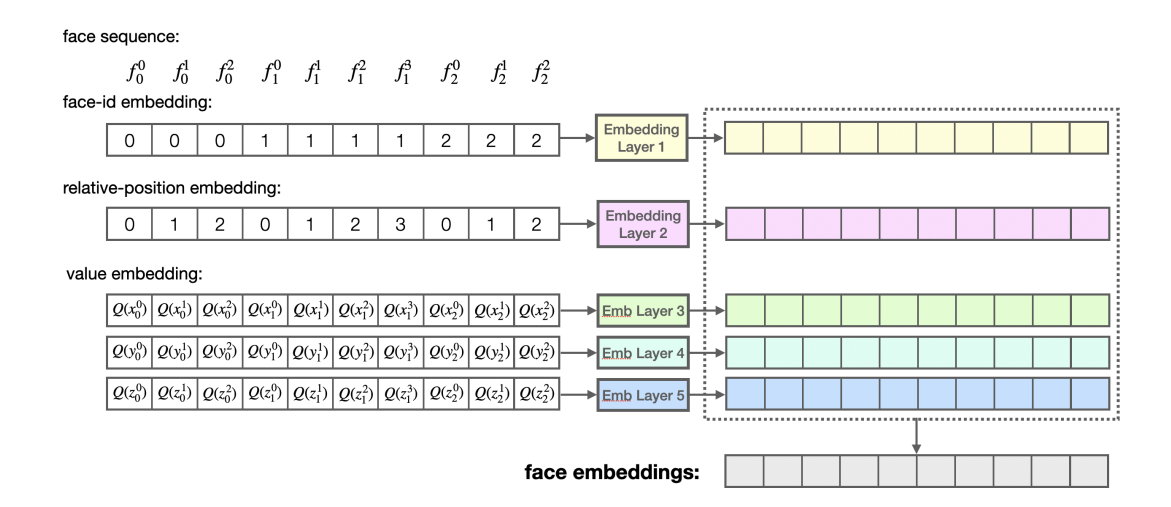


Figure 7: Illustration of the face embedding process, where f_i^j represents the j-th vertex of the i-th face in a mesh and $Q(\cdot)$ is a simple quantization function applied to the coordinate values. In this process, the resulting face embeddings for each token are synthesized by integrating three key components: the face-id embedding, the relative-position embedding, and the coordinate value embeddings for the vertices. Specifically, the face-id embedding layer (Embedding Layer 1) accommodates embeddings for up to the maximum number of faces + 1. The relative-position embedding layer (Embedding Layer 2) provides unique embeddings for each position within a face, supporting up to the maximum number of vertices within a face +1. The value embedding layers (Embedding Layers 3, 4, 5) supports embeddings for up to a maximum number of all vertices. Each of these embeddings is represented by a vector of 256 dimensions.

3.3. Mesh Generation

We employ multiple strategies for mesh generation during inference. Firstly, we use nucleus sampling to mitigate sample degradation. Additionally, when generating every single sequence during inference, we define token-level constraints to ensure a valid and meaningful token sequence. Moreover, once the full sequence has been generated, we perform a semantically informed validation, checking the logical structure and geometric consistency of elements such as floors and walls.

3.3.1. Nucleus Sampling

During inference we employ Nucleus sampling (Holtzman et al., 2019) as a technique to produce diverse outputs from the Transformer decoder. This method avoids degradation of sample quality by sampling from the top "nucleus" of the probability distribution — a subset with a cumulative probability above a certain threshold, discarding the tail of low probability options.

3.3.2. Enforcing Constraints for Mesh Generation

During one inference, both the vertex and face models are bound by specific rules, at the level of the token sequence, that ensure the validity of their predictions at each inference step. We thus introduce a series of checks in the form of binary masks to enforce hard constraints present in the mesh data, thus ruling out predictions that would lead to constraint violations. These checks include the proper placement of stopping tokens, the ordered progression of coordinate and index values, the uniqueness of vertices within faces, etc. If a prediction is discarded, the associated probability mass is redistributed evenly among the remaining valid options. For a detailed description of all constraints and their implementation, please refer to Appendix A.

3.3.3. Iterative generation strategy

During mesh generation, when reconstructing a new CAD model from a 3D point cloud, our approach follows a two-stage iterative process: first vertex generation, then face generation, ensuring that each stage adheres to the outlined validity protocols. Due to the inherent diversity in the sampled predictions, however, not all semantically valid samples necessarily satisfy the requirements we impose on the CAD models. This issue is common in generative modeling and is typically addressed with some form of aggregation, such as ensembling (Ke et al., 2024). We design an iterative procedure to interleave sampling the solution space with constraint checking – a form of rejection sampling. Importantly, our sampling procedure already implements low-level constraints on the token sequence to enforce the semantic correctness of the modeled sequences, as described in 3.3.2. The remaining, semantically informed constraints cannot be easily enforced through sampling and thus take the form of hardcoded rules. Consequently, the final CAD model is not generated in a single pass through both stages. Rather, we perform the described checks of intermediate results to enforce the rules and rerun stages when necessary:

Given a 3D point cloud, the algorithm commences by generating a set of vertices during the first stage. This initial step is subject to checking for the presence of the necessary stop tokens. Should the vertices not meet the required criteria, the algorithm regenerates vertices. Upon obtaining a valid set of vertices, the algorithm proceeds to the second stage, faces generation.

Faces are constructed from the vertices using a method that again incorporates validity checks. These checks account for the presence of the stop token as well as three further criteria that ensure structural integrity and coherence of the generated CAD model.

(1) The presence of a stop token indicates the completion of the face generation process for the

current set of vertices.

- (2) The faces that bound the building from below should cover the projection of the point cloud onto the ground (x, y) plane. Should this coverage be incomplete due to missing vertices or faces, the algorithm responds by initiating a new cycle of vertex generation, respectively undertaking additional iterations of face generation.
- (3) The integrity of the building structure is further validated by evaluating the connectivity between the edges of ground polygons and walls. All the edges of the ground polygon(s) should connect appropriately to the vertical edges of the walls. Its failure prompts the regeneration of faces.
- (4) Finally, the algorithm checks for the presence of diagonal lines on wall structures. If detected, these trigger additional iterations of face generation.

When the algorithm exhausts the maximum number of iterations for face generation without satisfying all criteria, it takes a step back and regenerates the vertices. This feedback mechanism between the two stages helps model the distribution of CAD models, as it allows us to incorporate the feedback from the face generation step and continue exploring the distribution of vertices before arriving at the final valid CAD model of the building. The algorithm is described in Alg. 1 in Appendix B.

4. Experiments

4.1. Dataset

3D point clouds. Our main dataset comes from Zurich, Switzerland. The LiDAR point clouds used for the building reconstruction come from the Swiss Federal Office of Topography (swisstopo, 2023). They include semantic category labels and are provided in LAS file format, with the points organized into square tiles each covering an area of $1km^2$. Following a modified version of the classification guidelines (Yan et al., 2015) established by the American Society for Photogrammetry and Remote Sensing (ASPRS), the points have been classified into six distinct classes: unclassified and temporary objects; ground; vegetation (further divided into low, medium, and high); buildings; water; bridges and viaducts. For our purpose, we exclusively utilize points labeled as buildings.

Polygonal meshes. The dataset comprising the corresponding polygonal mesh models comes from the open data released by the City of Zurich (Stadt Zurich, 2023). It includes 3D

representations of all current buildings within the city, crafted to Level of Detail 2 (LoD2). LoD2 models offer a refined depiction of buildings, including the precise geometry of roof structures and other major architectural features, but not minor facade details or interior structures. The data format varies, encompassing Drawing Interchange Format (.dxf), geodatabases (.gdb), GeoPackage (.gpkg), and others. For our analysis, we have processed all buildings into discrete polygonal meshes. Each building model is represented as a collection of vertices and flat faces that connect the vertices to form the building's exterior surface. Example meshes are shown in Fig. 8.

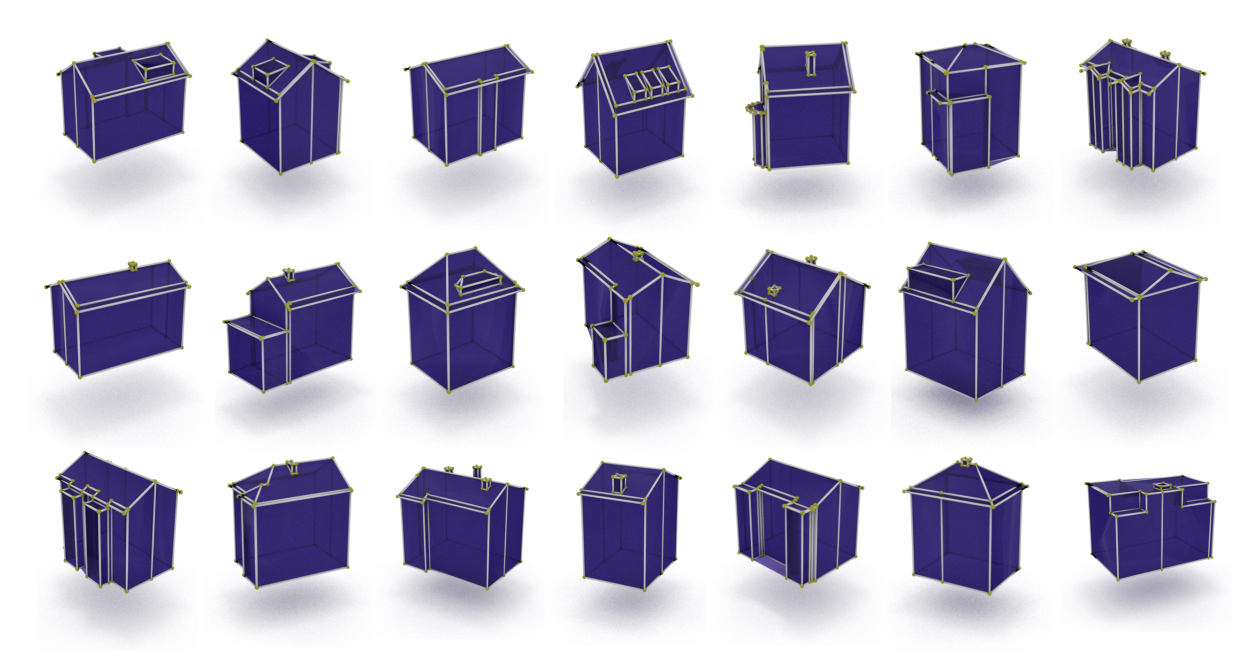


Figure 8: Examples of polygonal building meshes from the Zurich dataset.

Overall, the area used for our project, where the two data sources overlap, spans 9km by 8km. We partition that region into spatially disjoint training and test sets as depicted in Fig. 9.

Our work focuses on the learning-based reconstruction of 3D digital models from point clouds of individual buildings. Recognizing the complexity of segmenting the city-scale point cloud into individual buildings, we simplify the preprocessing of the dataset by sidestepping the segmentation problem. Instead, we first use the classification labels in the LiDAR scans to filter the data, then partition the points into subsets associated with separate buildings with the help of the reference footprints. Exemplary per-building point clouds are visualized in Fig. 10.

Additional datasets. We have also tested our method on datasets collected in two more cities:

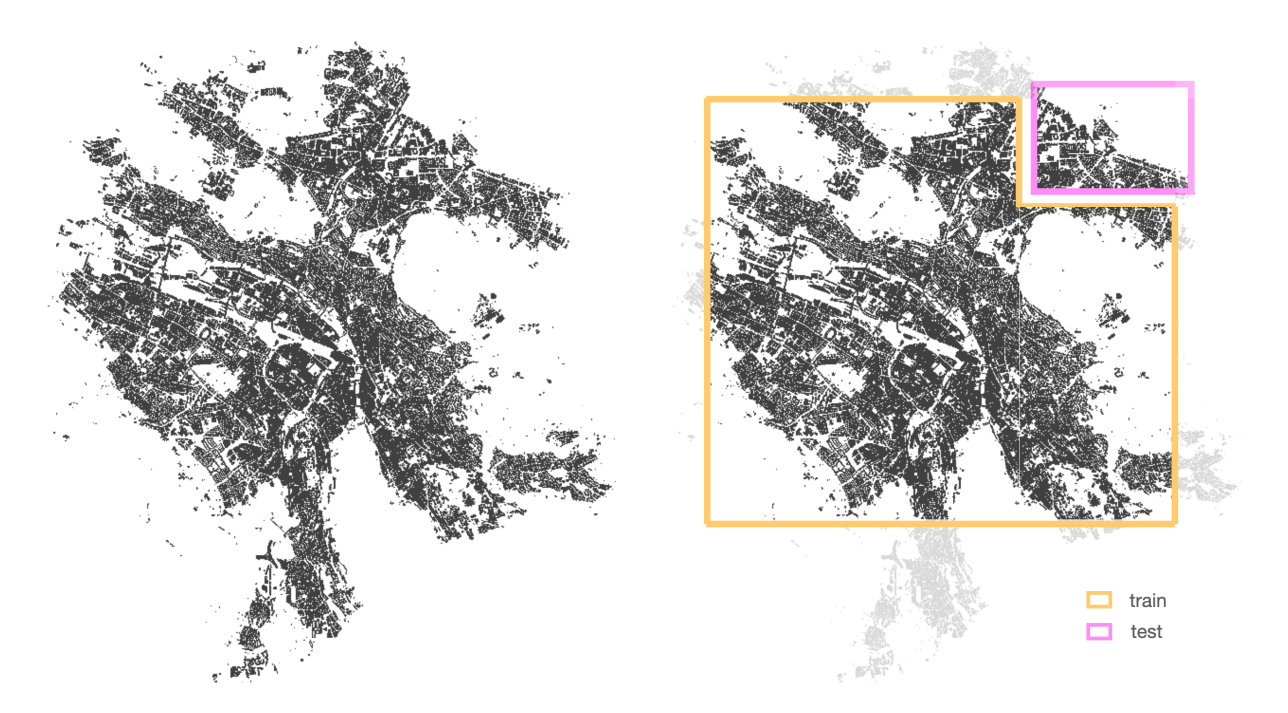


Figure 9: Zurich city buildings (left) and the corresponding train-test split dataset used in experiments (right).

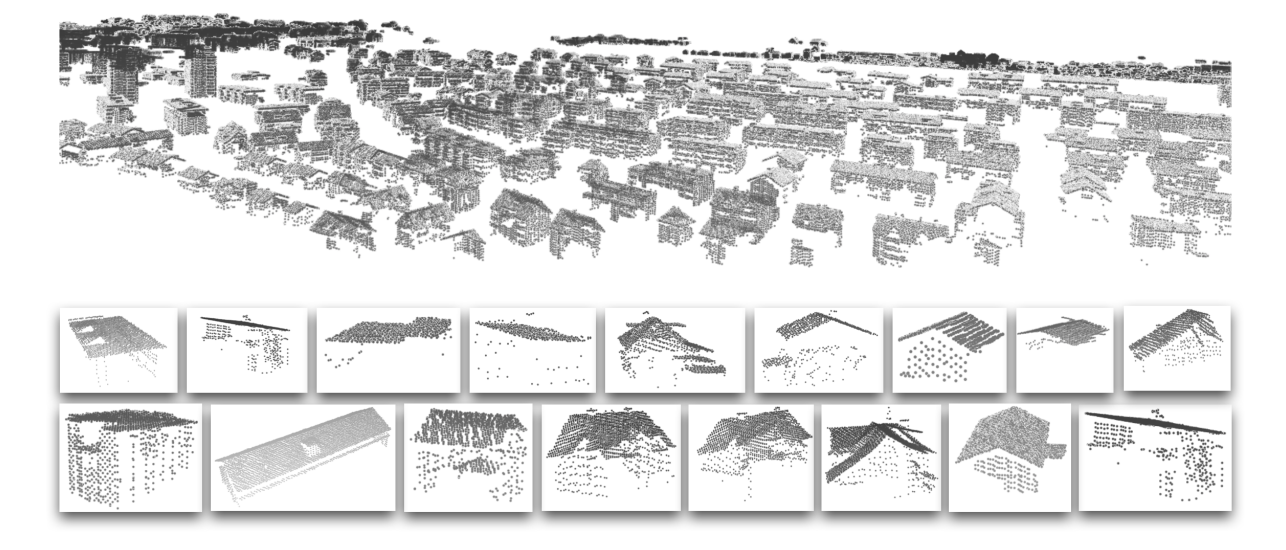


Figure 10: Point cloud samples from the Zurich dataset, featuring an overview at the top and detailed zoom-ins of individual building point clouds at the bottom.

Berlin, Germany and Tallinn, Estonia. The dataset from Berlin covers an area of $4 \text{km} \times 4 \text{km}$, comprising 69, 132 buildings for training and 7, 808 for testing. The source of both point clouds and corresponding polygonal meshes is the Open Data Initiative of the state of Berlin, available at Stadt Berlin (2021) and Berlin Business Location Center (2015). The Tallinn dataset spans a

3km×3km area, containing 33, 397 buildings for training and 2, 670 for testing. The LiDAR point clouds and meshes are both supplied by the Estonian Land Board for Spatial Data (Estonian Land Board, 2021). Examples are shown in Fig. 11.

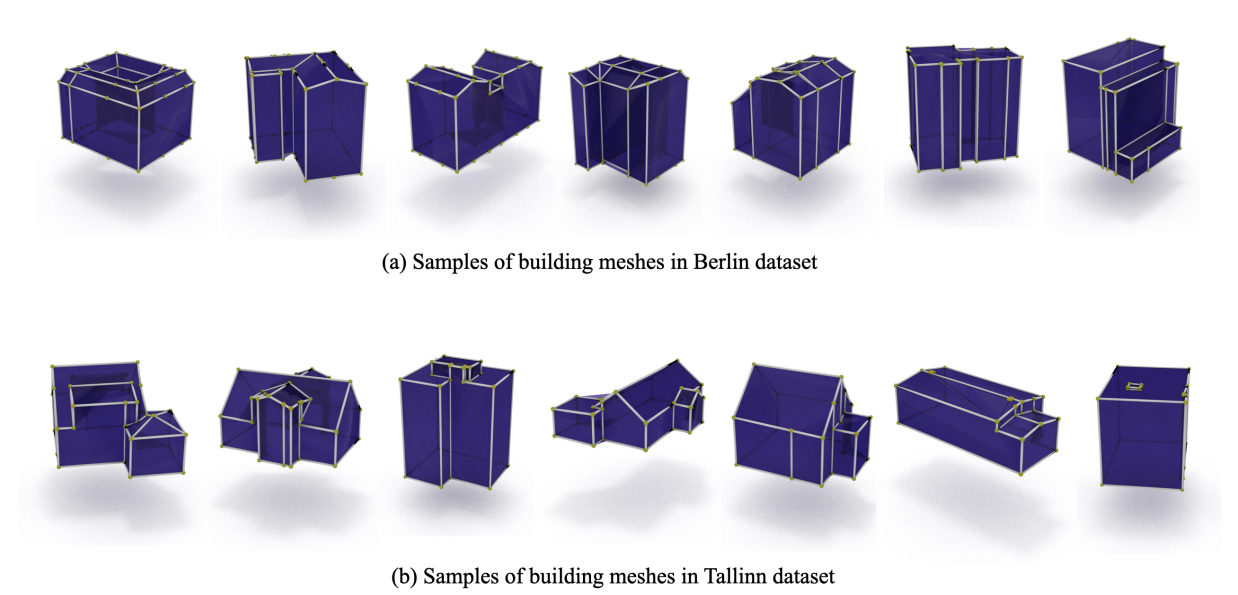


Figure 11: Examples of polygonal building meshes from the Berlin and Tallinn datasets.

4.2. Implementation details

To maintain reasonable computation complexity during training and inference, we exclude buildings that have in excess of 100 vertices, or over 500 faces. Moreover, we limit the processing to at most 10 resampling iterations in Alg. 1.

During training we employ data augmentation for increased robustness. Specifically, we apply random scaling along the x, y, and z axes by random factors within [0.8, 1.2]. Additionally, we further augment by rotating around the vertical (z) axis by random angles. Moreover we also apply slight perturbations to the vertex locations, with each vertex shifted by up to 10% of the object diameter.

We trained the vertex and face modules for 500,000 weight updates each, using the Adam optimizer with a batch size of 16, and with a gradient clipping at a maximum norm of 1.0 for stability. We adopt a cosine annealing scheme for the learning rate schedule, commencing from a maximum learning rate of 3×10^{-4} , while also applying a linear warm-up during the first 5000 steps. Dropout at a rate of 0.2 was applied in the training of both modules.

4.3. Evaluation metrics

To assess the fidelity of our reconstructed CAD models, we utilize three different distance metrics.

Mean Distance Error (MDE) serves as a metric to quantify the average deviation from the ground truth w.r.t. both vertices and surfaces. To compute the MDE on surfaces, we uniformly sample 10,000 points on the surface of the ground truth mesh and project them onto the nearest surface plane of the predicted mesh to obtain a set of point correspondences. The MDE is calculated as the mean Euclidean distance between corresponding points, so it measures the average spatial distance between the true and predicted surfaces.

Hausdorff distance is used to measure the maximum extent of deviation between the reconstructed surface and the ground truth mesh. It captures the maximum distance from a point on one surface to the closest point on the other surface, thus providing the worst-case scenario in terms of per-point error. The equation for the Hausdorff distance, where A and B represent the uniformly sampled 10,000 point sets from the ground truth and reconstructed surfaces respectively, is given by:

$$H(A,B) = \max \left\{ \sup_{a \in A} \left(\inf_{b \in B} d(a,b) \right), \sup_{b \in B} \left(\inf_{a \in A} d(a,b) \right) \right\},\,$$

with $d(\cdot, \cdot)$ the Euclidean distance.

Chamfer distance is also calculated, to evaluate the average closest point distance between vertex sets and surfaces. This metric measures the minimum deformation needed "warp" the prediction to the ground truth, and gives a sense of the overall shape difference. The distance computation for surfaces follows the same sampling strategy as above. The Chamfer distance is defined as follows:

$$C(A, B) = \frac{1}{|A|} \sum_{a \in A} \sum_{b \in B} \min d(a, b) + \frac{1}{|B|} \sum_{b \in B} \sum_{a \in A} \min d(b, a).$$

Precision, Recall and F1-score for vertices and edges. To further evaluate the performance of vertex and edge reconstruction within our model, we measure precision, recall, and F1-score for vertices and edges. These metrics provide a measure of reconstruction accuracy for the individual mesh elements, by counting what fraction of vertices or edges has been recovered within a set tolerance. The three metrics are computed under various distance

Table 1: Evaluation on vertex prediction quality with different methods: City3D (Huang et al., 2022), 2.5D Dual Contour (Zhou and Neumann, 2010) and Ours. Best values are bold.

| | precision ↑ | recall ↑ | F1-score ↑ | Chamfer distance \downarrow |
|-------------------|-------------|----------|------------|-------------------------------|
| City3D | 0.6717 | 0.7364 | 0.6804 | 0.9387 |
| 2.5D Dual Contour | 0.2899 | 0.5060 | 0.3553 | 1.4006 |
| Our Vertex-module | 0.8928 | 0.8617 | 0.8677 | 0.5816 |

thresholds, in order to also evaluate how the model performance varies with different tolerances for vertex and edge alignment.

4.4. Quantitative results

We compare our method against two representative baselines, City3D (Huang et al., 2022) and the 2.5D Dual Contouring method (Zhou and Neumann, 2010).

First, we assess the accuracy of vertex prediction. The precision, recall, and F1-score metrics indicate a high degree of correctness in identifying vertices. With a chosen true positive threshold set at 1m, deemed reasonable for the accuracy requirements of building reconstruction, these metrics are reported in Tab. 1. We also plot the F1-score curve against varying thresholds in Fig. 13a. Our approach maintains a higher score across different conditions meaning that it consistently retrieves vertices and edges more correctly, across a range of geometric accuracy requirements. Further, the lower Chamfer distance confirms the better precision of the reconstructed vertex locations, meaning that the building surfaces reconstructed by our method are geometrically closer to the ground truth shapes. We also examine the absolute error in the predicted number of vertices relative to the ground truth. Compared to other methods, the histogram Fig. 12a reveals that a larger fraction of all samples have small error, implying that our method gets closest to the true vertex counts.

Next, we assess the absolute errors in the lengths of edges and the areas of faces, as illustrated in Fig. 12c and Fig. 12d, respectively. The errors with our method are more concentrated near zero for both metrics, indicating that it most precisely reconstructs edge and face dimensions.

Furthermore, the F1-score of the proposed method remains higher than those of the two baselines across a wide range of tolerance values, Fig. 13b, meaning that, at any given accuracy threshold it achieves a better balance between recall and precision.

Finally, in terms of surface quality metrics, Tab. 2, our method achieves the lowest mean

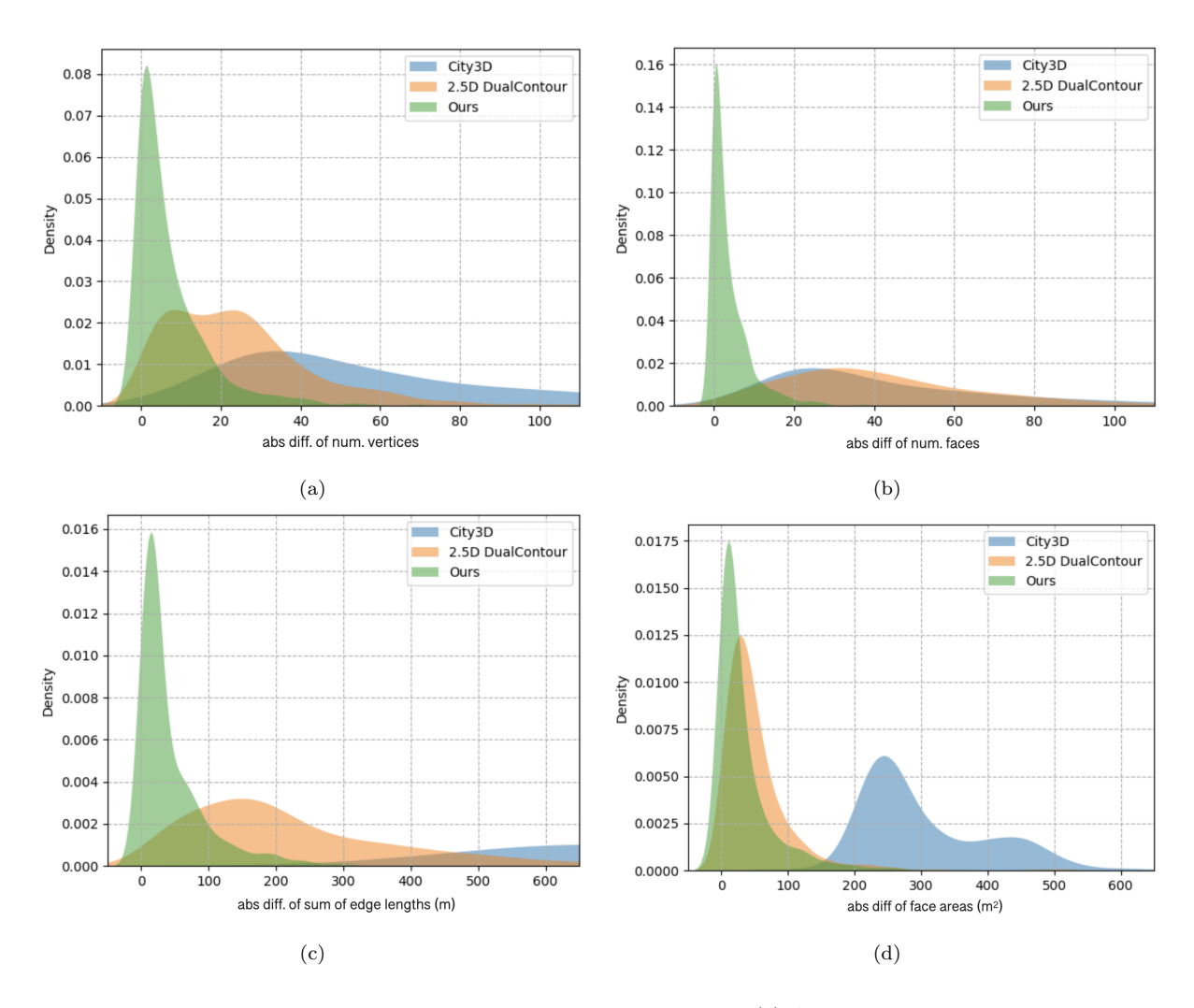


Figure 12: Error distributions with different reconstruction methods. (a) Absolute difference of vertex counts. (b) Absolute difference of face counts. (c) Absolute difference of sum of edge lengths in meters. (d) Absolute difference of face areas in square meters.

Table 2: Various errors (m) of reconstruction with different methods: City3D (Huang et al., 2022), 2.5D Dual Contour (Zhou and Neumann, 2010) and Ours. Best values are bold.

| | $	ext{MDE}\downarrow$ | Hausdorff distance \downarrow | Chamfer distance \downarrow |
|------------------|-----------------------|---------------------------------|-------------------------------|
| City3D | 0.3046 | 1.4723 | 0.3708 |
| 2.5D DualContour | 0.3646 | 1.9157 | 0.4368 |
| Ours | 0.2542 | 1.1200 | 0.3060 |

distance error, Hausdorff distance, and Chamfer distance w.r.t. the ground truth models. These metrics collectively emphasize the fidelity of our reconstruction, with the mean distance highlighting average deviation, the Hausdorff distance indicating maximum discrepancy, and the Chamfer distance reflecting overall shape similarity.

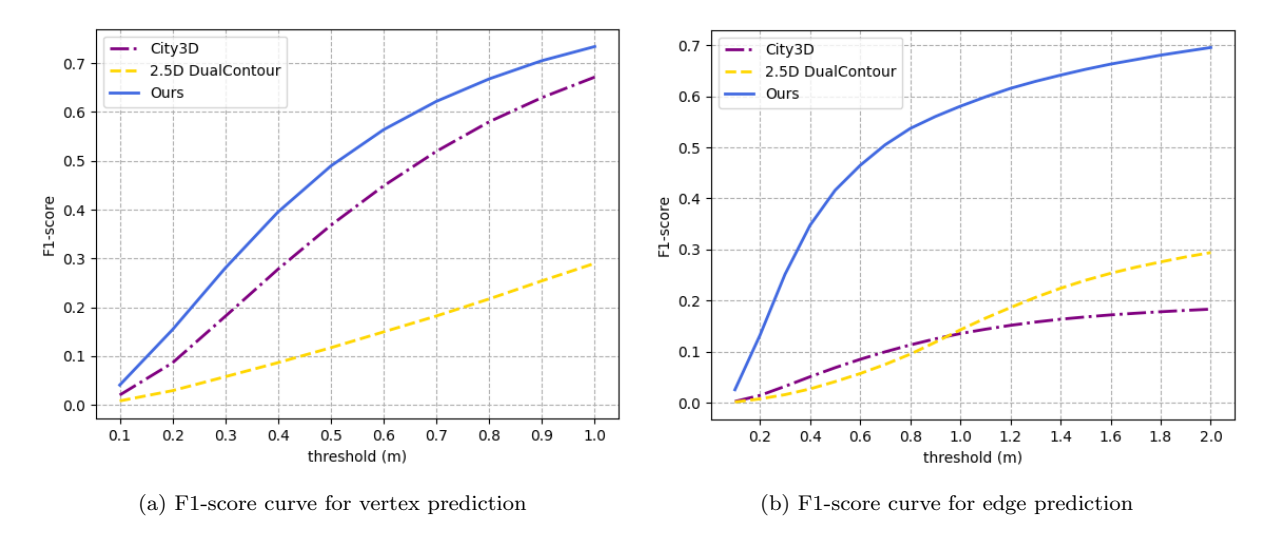


Figure 13: F1-score curves for vertex and edge prediction with different algorithms.

4.5. Qualitative results

When visually inspecting the reconstructed building models, as depicted in Fig. 14, we observe that our method effectively deals with the common issue of incomplete input point clouds, characterized by denser points on roofs and sparser points on walls. The generative model can reconstruct fine structural details, such as thin chimneys, even from minimal evidence. In contrast, alternative methods often yield overly simplified models that omit such details, or they create models with an excessive number of spurious edges. We also present a gallery of perspective views with many reconstructed building blocks in Fig. 15, comparing the reconstruction quality of different approaches. Further results for the entire test region of Zurich are shown in Fig. 17.

As a particular feature, our dataset includes numerous houses with roof overhangs — a feature that existing methods typically struggle to replicate. The sequential polygon prediction in our generative model successfully captures these overhangs, as shown in Fig. 15 (bottom), underscoring its ability to handle varied meshes geometries when supervised with appropriate reference data.

Failure cases. Figure 16 shows instances where our models did not yield the desired results. These failures usually fall into two categories. The first one are erroneous vertex

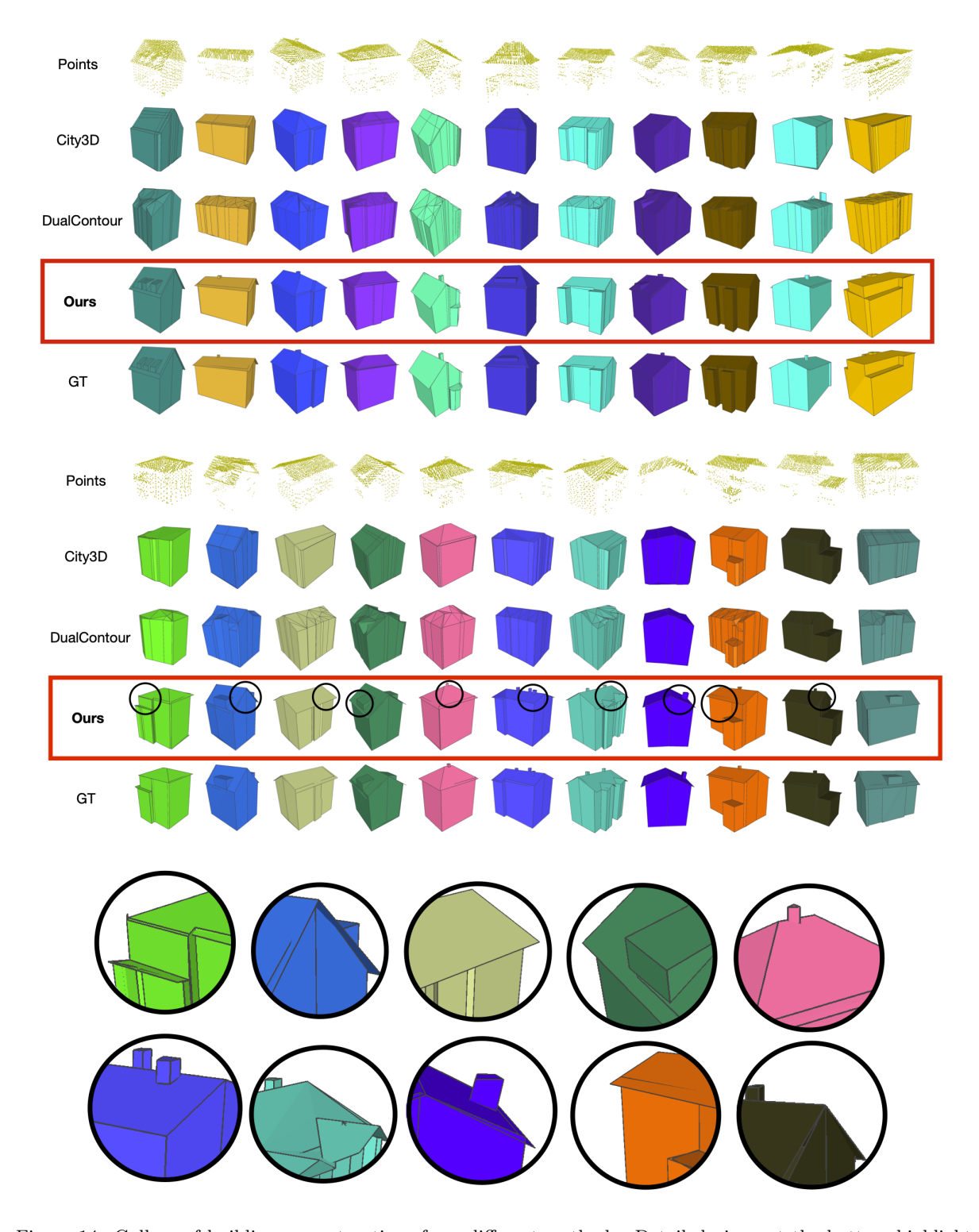


Figure 14: Gallery of building reconstructions from different methods. Detailed views at the bottom highlight the ability of our method to reconstruct detailed features such as roof overhangs and chimneys.

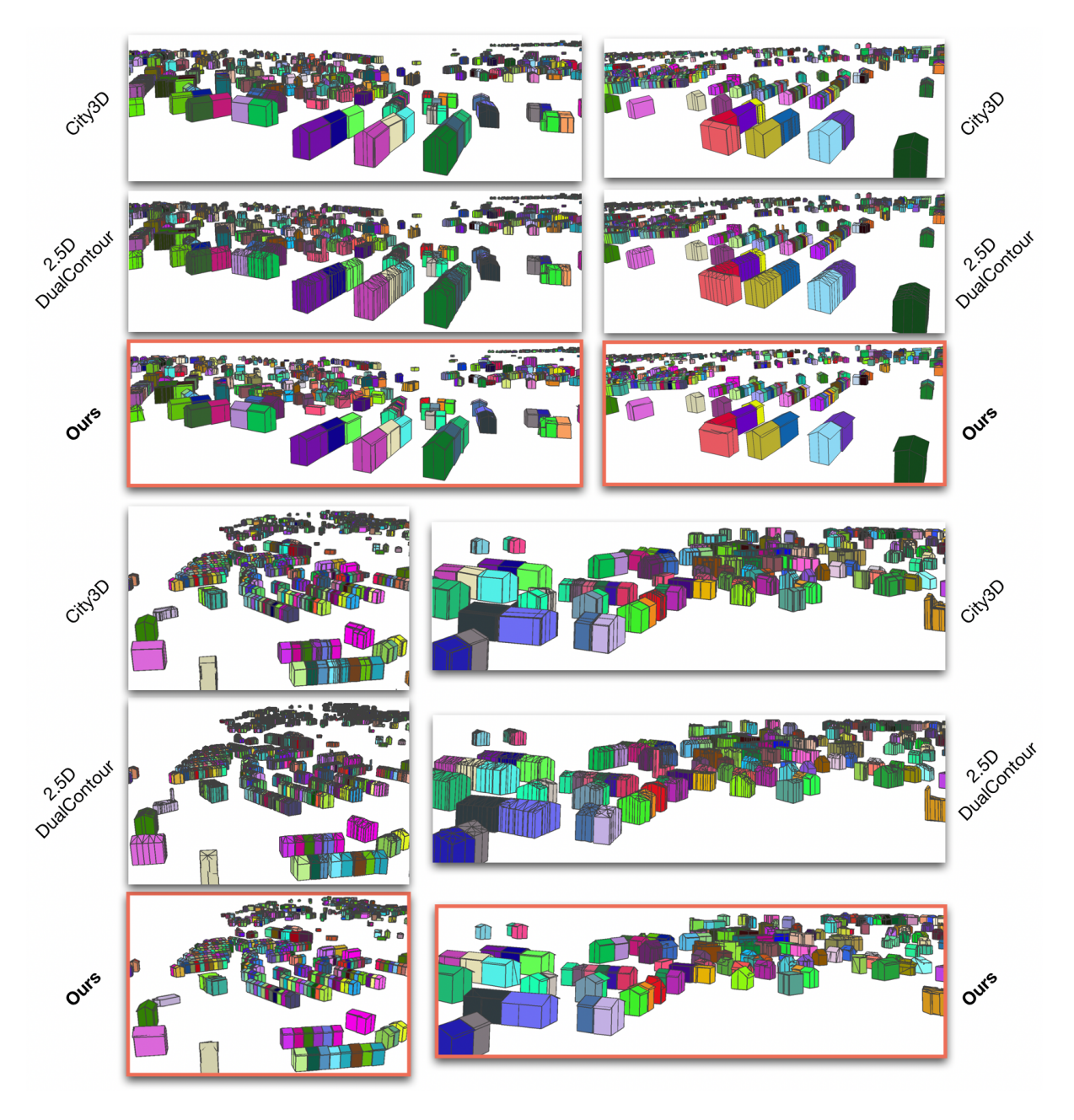


Figure 15: Gallery of reconstructed building blocks. Each vertical triplet of images showcases the reconstruction results from City3D, 2.5D DualContour, and our method, respectively.

predictions: omitted or misplaced vertices inevitably lead to significant deviations from the ground truth, since vertices are the geometric basis for the mesh faces. The other main failure mode is inadequate face generation. Unsurprisingly, the model performance tends to decline with increasingly complex building geometry. The generation of faces proves particularly challenging for intricate roof designs that result in a scarcity of input points on finer sub-structures.

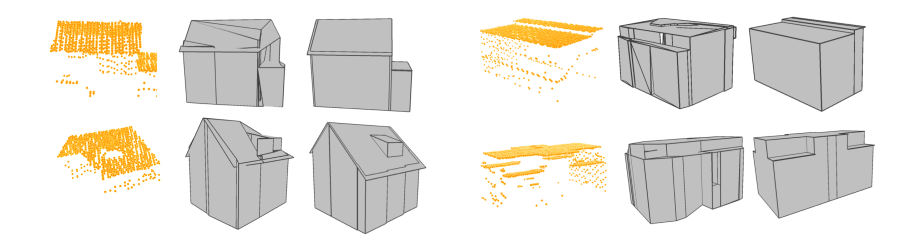


Figure 16: Examples (input, reconstruction and reference) with large reconstruction errors.

Table 3: Ablation studies

| | MDE ↓ | Hausdorff distance \downarrow | Chamfer distance \downarrow |
|-----------------------------|--------|---------------------------------|-------------------------------|
| Ours: alternative vertex | 0.1885 | 0.9695 | 0.2337 |
| Ours: w/o constraints | 0.1624 | 0.7521 | 0.2197 |
| Ours: single inference | 0.1998 | 1.2584 | 0.2554 |
| Ours: w/o data augmentation | 0.2542 | 1.1296 | 0.3060 |
| Ours: full | 0.1554 | 0.7488 | 0.2149 |

4.6. Ablation Study

Vertex Module. For the first ablation study, we investigate the importance of the sequential, autoregressive prediction. To do so we design an alternative method for vertex generation. The point cloud encoder stays the same, but instead of instead of the sequential prediction it is followed by a decoder that predicts a set of unordered 3D vertex coordinates, also via a series of Transformer blocks. The inputs to the decoder are the point cloud features and a set of query embeddings. The decoder transforms those inputs into a new set of features. From those features, a prediction head in the form of a three-layer perceptron extracts 3D vertex coordinates, and another prediction head extracts classification scores that indicate the likelihood of each vertex being present in the reconstruction. The unordered model is supervised with a combination of an L2 loss for the coordinates and a binary cross-entropy loss for the classification scores. The set of vertices to be passed on to the subsequent face module is determined by thresholding the classification score at 0.5. Results are presented in Tab. 3, labeled as "Ours: alternative vertex". They indicate a decline across all quality metrics, suggesting that the autoregressive design of the original generative model is crucial to adequately capture the spatial relationships between vertices, and more conducive to the subsequent mesh face reconstruction.

Token-level constraints. Our method integrates several constraints that guide the generation of vertices and faces, ensuring the resulting 3D models adhere to specified geometric rules and architectural principles. To evaluate the contribution of these token-level constraints to the quality of the reconstructed models, we conducted an ablation study where we removed the plausibility checks from the shape generation process. When not bound by the constraints, the transformer network operates with greater freedom, providing insights into its intrinsic capabilities and the underlying data representation. Without constraints, the generation pipeline IS solely dependent on the patterns learned from the training data, without additional guidance to refine the placement of vertices or the construction of faces. The results are shown in Tab. 3 as "Ours: w/o constraints". We observe a decrease across all quality metrics upon removing the token-level constraints; indicating that, although our network has extracted useful patterns from the training data, it is not constrained tightly enough by the learned patterns. **Single inference.** We also conducted an ablation study where we disabled the iterative generation that, per default, is part of our model. The iteration scheme is designed to repeatedly generate complete building hypotheses until the output fulfills the predefined set of rules, ensuring the validity of the predicted model. To understand the significance of that procedure, we modified it to generate a single result for each test sample, with the token-level constraints enabled, but without regard for the validity of the predicted full building model. The corresponding quality metrics are shown in Tab. 3 as "Ours: single inference". They point to a marked decline in performance if we forgo the iterative generation and limit ourselves to single-shot generation per sample, irrespective of semantic plausibility. This finding highlights the importance of the quality filter and associated iteration scheme to iteratively refine the reconstruction.

Data augmentation. During the training phase, data augmentation techniques, specifically scaling, rotation around the z-axis, and adding noise, were employed. An ablation study was conducted to evaluate their impact. The results, as detailed in Tab. 3 ("Ours: w/o data augmentation"), show a significant quality gain attributable to data augmentation. It is thus likely that our model is still not trained to its full performance and would benefit from even larger quantities of training data, especially given the favorable scaling properties of transformer architectures.

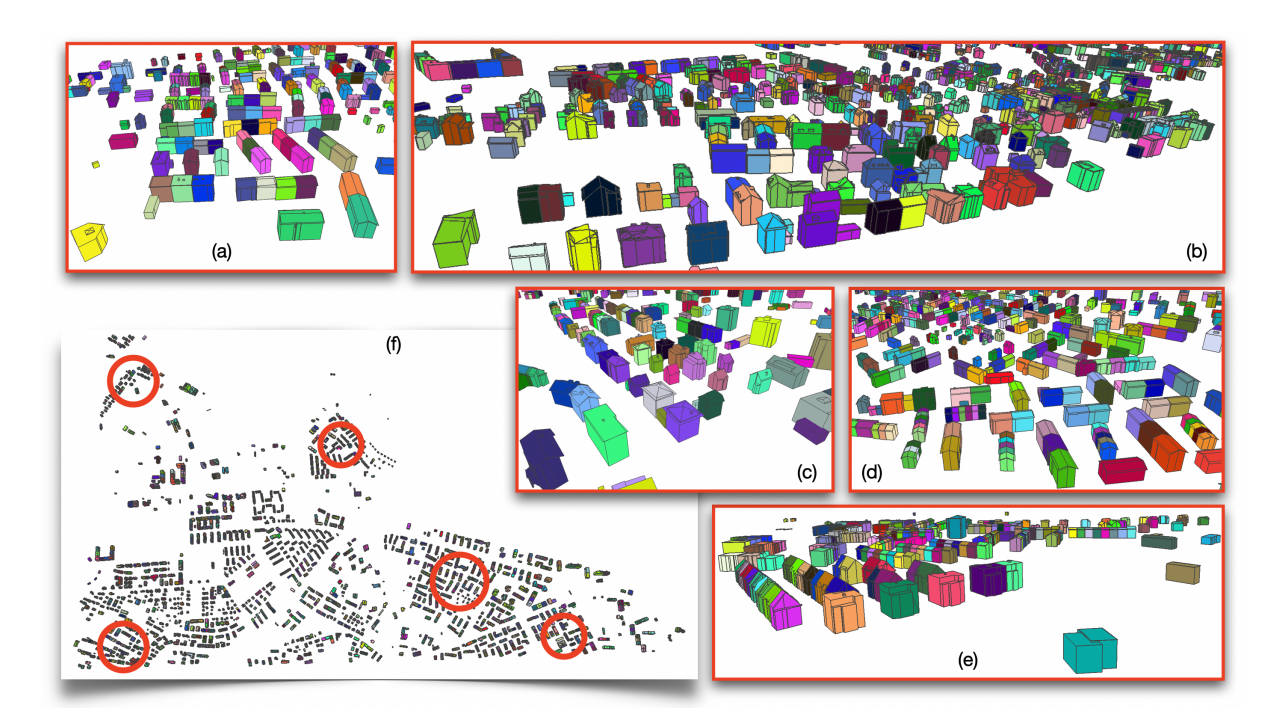


Figure 17: Reconstructed building blocks in Zurich. (f): Reconstruction of a $3km \times 2km$ area in Zurich. (a) - (e) Magnified views of selected regions.

4.7. Results of reconstructing other cities

Beyond Zurich, we have also applied our method to LiDAR data from Berlin and Tallinn, retraining the models specifically for each city's datasets. The results are depicted in Fig. 18 and Fig. 19. Despite the variations in building shapes between different cities, the reconstruction outcomes consistently exhibit high geometric quality.

4.8. Discussion

Several challenges remain when it comes to handling complex roofs and fine architectural elements, particularly if the associated point clouds are relatively sparse. Future efforts could explore ways to enhance the model's sensitivity to small roof structures, potentially through more powerful point cloud encoders, or through architectural innovations that promote even better contextual reasoning. A conceptual limitation of our current approach are the independent prediction modules for vertices and faces, which may hamper the synergies between vertex and face processing. Future extensions should seek to integrate the two subtasks more tightly, which could potentially improve reconstruction accuracy while reducing the computational cost of inference. Finally, we have concentrated on the reconstruction step. For a

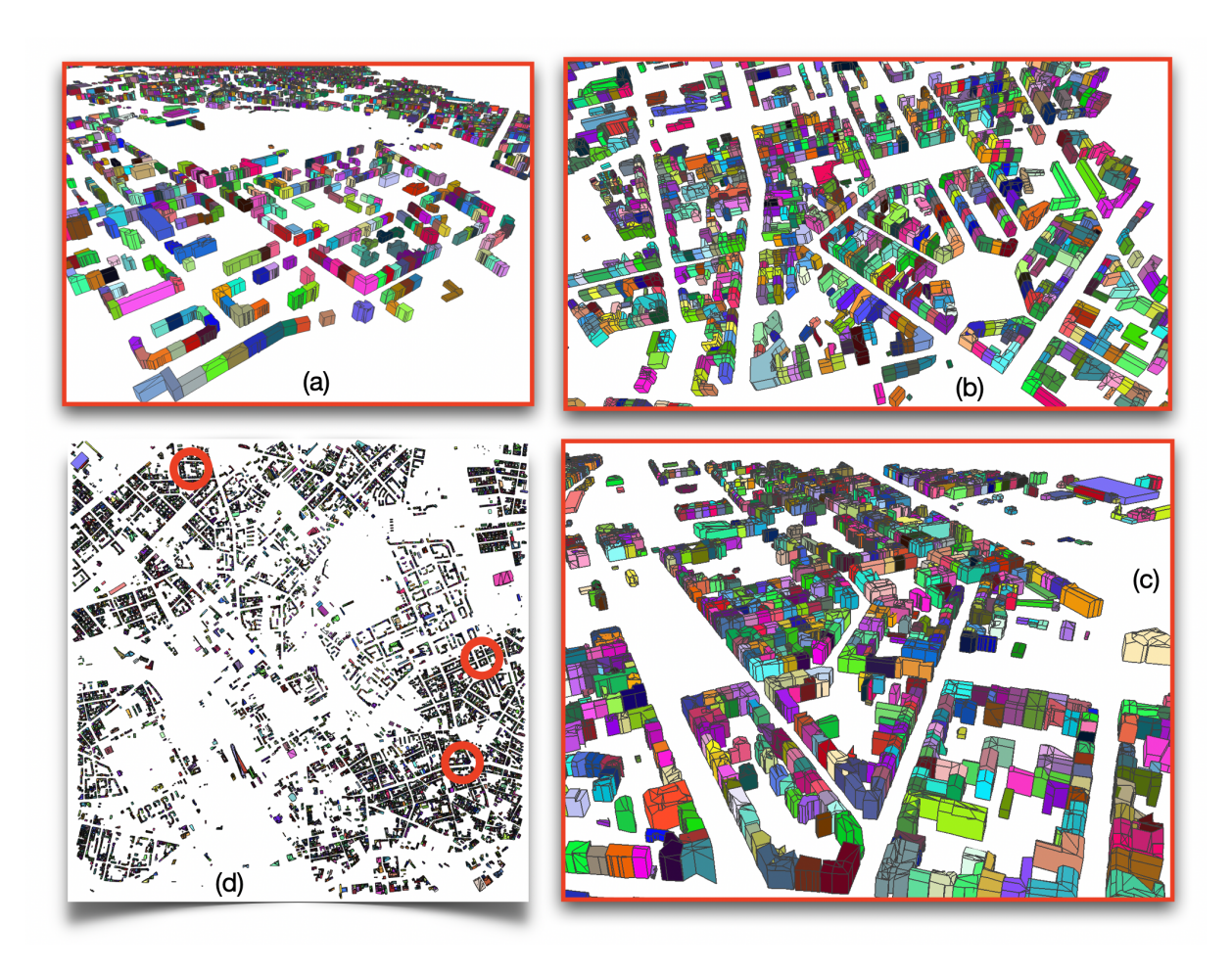


Figure 18: Reconstructed building blocks in Berlin. (d) Reconstruction of a $4km \times 4km$ area in Berlin. (a) - (c) Magnified views of selected regions.

fully automatic pipeline, future research will be needed to reliably segment the raw scan data into individual building units. That step, which is a prerequisite for a complete, highly automated urban modelling tool, can draw from the rich literature on detection and segmentation in 3D point clouds.

5. Conclusion

We have studied the task of automatically reconstructing 3D polygonal mesh models of buildings from airborne LiDAR point clouds, and have proposed an autoregressive, generative model based on the transformer architecture. The model consists of two parts, a vertex module for sequential vertex generation and a subsequent face module to that connects vertices to mesh faces. When combined with geometric plausibility checks and rejection sampling, the novel

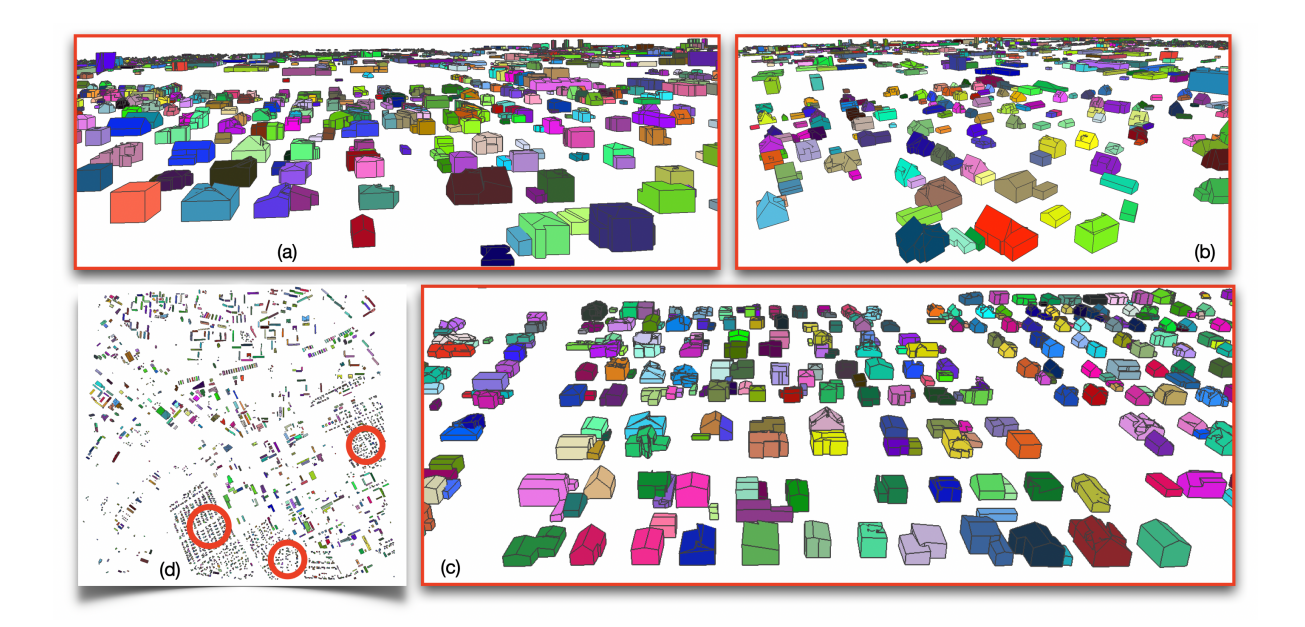


Figure 19: Reconstructed building blocks in Tallinn. (d) Reconstruction of a $3km \times 3km$ area in Tallinn. (a) - (c) Magnified views of selected regions.

model consistently outperforms both a classical optimization-based and a recent learning-based baseline across a range of performance metrics.

References

Badki, A., Gallo, O., Kautz, J., Sen, P., 2020. Meshlet priors for 3d mesh reconstruction. In: IEEE/CVF Conference on Computer Vision and Pattern Recognition (CVPR). pp. 2849–2858.

Berlin Business Location Center, 2015. Stadt Berlin Business Location Center. https://www.businesslocationcenter.de/en/economic-atlas/download-portal.

Boissonnat, J.-D., Oudot, S., 2005. Provably good sampling and meshing of surfaces. Graphical Models 67 (5), 405–451.

Botsch, M., Kobbelt, L., Pauly, M., Alliez, P., Lévy, B., 2010. Polygon mesh processing. CRC Press.

Brenner, C., Haala, N., Fritsch, D., 2001. Towards fully automated 3d city model generation.

Chen, J., Chen, B., 2008. Architectural modeling from sparsely scanned range data. International Journal of Computer Vision 78, 223–236.

Chen, Q., 2007. Airborne lidar data processing and information extraction. Photogrammetric Engineering & Remote Sensing 73 (2), 109.

- Chen, Z., Ledoux, H., Khademi, S., Nan, L., 2022. Reconstructing compact building models from point clouds using deep implicit fields. ISPRS Journal of Photogrammetry and Remote Sensing 194, 58–73.
- Chen, Z., Shi, Y., Nan, L., Xiong, Z., Zhu, X. X., 2023. PolyGNN: Polyhedron-based graph neural network for 3d building reconstruction from point clouds. arXiv preprint arXiv:2307.08636.
- Chen, Z., Tagliasacchi, A., Zhang, H., 2020. BSP-Net: Generating compact meshes via binary space partitioning. In: IEEE/CVF Conference on Computer Vision and Pattern Recognition (CVPR). pp. 45–54.
- Chen, Z., Zhang, H., 2019. Learning implicit fields for generative shape modeling. In: IEEE/CVF Conference on Computer Vision and Pattern Recognition (CVPR). pp. 5939–5948.
- Cheng, L., Gong, J., Li, M., Liu, Y., 2011. 3d building model reconstruction from multi-view aerial imagery and lidar data. Photogrammetric Engineering & Remote Sensing 77 (2), 125–139.
- Choy, C., Gwak, J., Savarese, S., 2019. 4d spatio-temporal convnets: Minkowski convolutional neural networks. In: IEEE/CVF Conference on Computer Vision and Pattern Recognition (CVPR). pp. 3075–3084.
- Dai, A., Ritchie, D., Bokeloh, M., Reed, S., Sturm, J., Nießner, M., 2018. ScanComplete: Large-scale scene completion and semantic segmentation for 3d scans. In: IEEE/CVF Conference on Computer Vision and Pattern Recognition (CVPR). pp. 4578–4587.
- Dorninger, P., Pfeifer, N., 2008. A comprehensive automated 3d approach for building extraction, reconstruction, and regularization from airborne laser scanning point clouds. Sensors 8 (11), 7323–7343.
- Estonian Land Board, 2021. Estonian Land Board. https://daten.berlin.de/datensaetze/airborne-laserscanning-als-primre-3d-laserscan-daten-wms.
- Fabio, R., et al., 2003. From point cloud to surface: the modeling and visualization problem. International Archives of Photogrammetry, Remote Sensing and Spatial Information Sciences 34 (5), W10.
- Groueix, T., Fisher, M., Kim, V. G., Russell, B. C., Aubry, M., 2018. A papier-mâché approach to learning 3d surface generation. In: IEEE Conference on Computer Vision and Pattern Recognition (CVPR). pp. 216–224.
- Guerrero, P., Kleiman, Y., Ovsjanikov, M., Mitra, N. J., 2018. PCPNet: learning local shape properties from raw point clouds. In: Computer Graphics Forum. Vol. 37. pp. 75–85.

- Guo, H., Liu, S., Pan, H., Liu, Y., Tong, X., Guo, B., 2022. ComplexGen: CAD reconstruction by B-rep chain complex generation. ACM Transaction on Graphics 41 (4), 1–18.
- Gupta, K., 2020. Neural mesh flow: 3d manifold mesh generation via diffeomorphic flows. University of California, San Diego.
- Halla, N., 1999. Virtual city models from laser altimeter and 2d map data. Photogrammetric Engineering & Remote Sensing 65 (7), 787–795.
- Holtzman, A., Buys, J., Du, L., Forbes, M., Choi, Y., 2019. The curious case of neural text degeneration. arXiv preprint arXiv:1904.09751.
- Hoppe, H., DeRose, T., Duchamp, T., McDonald, J., Stuetzle, W., 1992. Surface reconstruction from unorganized points. In: Conference on Computer Graphics and Interactive Techniques. pp. 71–78.
- Huang, H., Brenner, C., Sester, M., 2013. A generative statistical approach to automatic 3d building roof reconstruction from laser scanning data. ISPRS Journal of Photogrammetry and Remote Sensing 79, 29–43.
- Huang, J., Stoter, J., Peters, R., Nan, L., 2022. City3D: Large-scale building reconstruction from airborne LiDAR point clouds. Remote Sensing 14 (9), 2254.
- Jiang, C., Huang, J., Kashinath, K., Marcus, P., Niessner, M., et al., 2019. Spherical CNNs on unstructured grids. arXiv preprint arXiv:1901.02039.
- Jiang, C., Huang, J., Tagliasacchi, A., Guibas, L. J., 2020. ShapeFlow: Learnable deformation flows among 3d shapes. Advances in Neural Information Processing Systems (NeurIPS) 33, 9745–9757.
- Jiang, C., Marcus, P., et al., 2017. Hierarchical detail enhancing mesh-based shape generation with 3d generative adversarial network. arXiv preprint arXiv:1709.07581.
- Kada, M., McKinley, L., 2009. 3d building reconstruction from lidar based on a cell decomposition approach. International Archives of Photogrammetry, Remote Sensing and Spatial Information Sciences 38 (Part 3), W4.
- Kazhdan, M., Bolitho, M., Hoppe, H., 2006. Poisson surface reconstruction.
- Ke, B., Obukhov, A., Huang, S., Metzger, N., Daudt, R. C., Schindler, K., 2024. Repurposing diffusion-based image generators for monocular depth estimation.
- Labatut, P., Pons, J.-P., Keriven, R., 2009. Hierarchical shape-based surface reconstruction for dense multi-view stereo. In: IEEE International Conference on Computer Vision Workshops (ICCVW). pp. 1598–1605.

- Lafarge, F., Alliez, P., 2013. Surface reconstruction through point set structuring. In: Computer Graphics Forum. Vol. 32. pp. 225–234.
- Lafarge, F., Mallet, C., 2012. Creating large-scale city models from 3d-point clouds: a robust approach with hybrid representation. International Journal of Computer Vision 99, 69–85.
- Li, X., Liu, C., Wang, Z., Xie, X., Li, D., Xu, L., 2020. Airborne LiDAR: state-of-the-art of system design, technology and application. Measurement Science and Technology 32 (3), 032002.
- Li, Z., Shan, J., 2022. Ransac-based multi primitive building reconstruction from 3d point clouds. ISPRS Journal of Photogrammetry and Remote Sensing 185, 247–260.
- Liao, Y., Donne, S., Geiger, A., 2018. Deep marching cubes: Learning explicit surface representations.
 In: IEEE Conference on Computer Vision and Pattern Recognition (CVPR). pp. 2916–2925.
- Liu, X., 2008. Airborne LiDAR for DEM generation: some critical issues. Progress in Physical Geography 32 (1), 31–49.
- Liu, Y., Obukhov, A., Wegner, J. D., Schindler, K., 2023. Point2cad: Reverse engineering cad models from 3d point clouds. arXiv preprint arXiv:2312.04962.
- Ma, Q., Saito, S., Yang, J., Tang, S., Black, M. J., 2021. SCALE: Modeling clothed humans with a surface codec of articulated local elements. In: IEEE/CVF Conference on Computer Vision and Pattern Recognition (CVPR). pp. 16082–16093.
- Maas, H.-G., Vosselman, G., 1999. Two algorithms for extracting building models from raw laser altimetry data. ISPRS Journal of Photogrammetry and Remote Sensing 54 (2-3), 153–163.
- Martin-Brualla, R., Radwan, N., Sajjadi, M. S., Barron, J. T., Dosovitskiy, A., Duckworth, D., 2021. NeRF in the wild: Neural radiance fields for unconstrained photo collections. In: IEEE/CVF Conference on Computer Vision and Pattern Recognition (CVPR). pp. 7210–7219.
- Mescheder, L., Oechsle, M., Niemeyer, M., Nowozin, S., Geiger, A., 2019. Occupancy networks: Learning 3d reconstruction in function space. In: IEEE/CVF Conference on Computer Vision and Pattern Recognition (CVPR). pp. 4460–4470.
- Mildenhall, B., Srinivasan, P. P., Tancik, M., Barron, J. T., Ramamoorthi, R., Ng, R., 2021. NeRF: Representing scenes as neural radiance fields for view synthesis. Communications of the ACM 65 (1), 99–106.
- Nan, L., Wonka, P., 2017. PolyFit: Polygonal surface reconstruction from point clouds. In: IEEE International Conference on Computer Vision (ICCV). pp. 2353–2361.

- Nash, C., Ganin, Y., Eslami, S. A., Battaglia, P., 2020. PolyGen: An autoregressive generative model of 3d meshes. In: International Conference on Machine Learning (ICML). pp. 7220–7229.
- Park, J. J., Florence, P., Straub, J., Newcombe, R., Lovegrove, S., 2019. DeepSDF: Learning continuous signed distance functions for shape representation. In: IEEE/CVF Conference on Computer Vision and Pattern Recognition (CVPR). pp. 165–174.
- Poullis, C., You, S., 2009. Automatic reconstruction of cities from remote sensor data. In: IEEE Conference on Computer Vision and Pattern Recognition (CVPR). pp. 2775–2782.
- Poullis, C., You, S., Neumann, U., 2008. Rapid creation of large-scale photorealistic virtual environments. In: IEEE Virtual Reality Conference. pp. 153–160.
- Salman, N., Yvinec, M., Mérigot, Q., 2010. Feature preserving mesh generation from 3d point clouds.
 In: Computer Graphics Forum. Vol. 29. pp. 1623–1632.
- Sampath, A., Shan, J., 2007. Building boundary tracing and regularization from airborne LiDAR point clouds. Photogrammetric Engineering & Remote Sensing 73 (7), 805–812.
- Sampath, A., Shan, J., 2009. Segmentation and reconstruction of polyhedral building roofs from aerial lidar point clouds. IEEE Transactions on Geoscience and Remote Sensing 48 (3), 1554–1567.
- Schindler, F., Wörstner, W., Frahm, J.-M., 2011. Classification and reconstruction of surfaces from point clouds of man-made objects. In: IEEE International Conference on Computer Vision Workshops (ICCVW). pp. 257–263.
- Schnabel, R., Wahl, R., Klein, R., 2007. Efficient RANSAC for point-cloud shape detection. Computer Graphics Forum 26 (2), 214–226.
- Stadt Berlin, 2021. Stadt Berlin Open Data. https://daten.berlin.de/datensaetze/airborne-laserscanning-als-primre-3d-laserscan-daten-wms.
- Stadt Zurich, 2023. Stadt Zurich Open Data. https://data.stadt-zuerich.ch/dataset.
- swisstopo, 2023. swisssurface3d. https://www.swisstopo.admin.ch/en/geodata/height/surface3d. html.
- van den Oord, A., Dieleman, S., Zen, H., Simonyan, K., Vinyals, O., Graves, A., Kalchbrenner, N., Senior, A., Kavukcuoglu, K., 2016a. Wavenet: A generative model for raw audio. arXiv preprint arXiv:1609.03499.
- van den Oord, A., Kalchbrenner, N., Kavukcuoglu, K., 2016b. Pixel recurrent neural networks. In: International Conference on Machine Learning (ICML). pp. 1747–1756.

- Van Kreveld, M., Van Lankveld, T., Veltkamp, R. C., 2011. On the shape of a set of points and lines in the plane. In: Computer Graphics Forum. Vol. 30. pp. 1553–1562.
- Vaswani, A., Shazeer, N., Parmar, N., Uszkoreit, J., Jones, L., Gomez, A. N., Kaiser, L., Polosukhin, I., 2017. Attention is all you need. Advances in Neural Information Processing Systems (NeurIPS) 30.
- Verdie, Y., Lafarge, F., Alliez, P., 2015. LOD generation for urban scenes. ACM Transactions on Graphics 34, 30.
- Verma, V., Kumar, R., Hsu, S., 2006. 3d building detection and modeling from aerial lidar data. In: IEEE Conference on Computer Vision and Pattern Recognition (CVPR). Vol. 2. pp. 2213–2220.
- Vinyals, O., Fortunato, M., Jaitly, N., 2015. Pointer networks. Advances in Neural Information Processing Systems (NeurIPS) 28.
- Vosselman, G., Dijkman, S., et al., 2001. 3d building model reconstruction from point clouds and ground plans. International Archives of Photogrammetry, Remote Sensing and Spatial Information Sciences 34 (3/W4), 37–44.
- Yan, W. Y., Shaker, A., El-Ashmawy, N., 2015. Urban land cover classification using airborne lidar data: A review. Remote Sensing of Environment 158, 295–310.
- Yang, M. Y., Förstner, W., et al., 2010. Plane detection in point cloud data. In: International Conference on Machine Control Guidance. Vol. 1. pp. 95–104.
- Zhou, Q.-Y., Neumann, U., 2010. 2.5D dual contouring: A robust approach to creating building models from aerial LiDAR point clouds. In: European Conference on Computer Vision (ECCV). pp. 115–128.
- Zhou, Q.-Y., Neumann, U., 2011. 2.5D building modeling with topology control. In: CVF Conference on Computer Vision and Pattern Recognition (CVPR). pp. 2489–2496.

Appendix A. Constraints for Mesh Generation

For the vertex module:

- (1) Stopping Token Placement: The sequence must place the stopping token only after an x-coordinate.
- (2) z-Coordinate: The sequence of sampled z-coordinates must be non-decreasing.
- (3) y-Coordinate: The subsequent y-coordinates should not decrease, if their corresponding z-coordinates are equal.
- (4) x-Coordinate: The subsequent x-coordinates must strictly increase when their y and z counterparts are equal to those preceding.

For the face module:

- (1) Face Index Progression: The first generated index of a new face must be greater or equal to the first index of the previous face.
- (2) Vertex Index Order: Within a face, subsequent vertex indices must be greater than the first index.
- (3) Vertex Uniqueness: All vertex indices within a face are required to be distinct.

Appendix B. Algorithm for Reconstruction and Validation of a Polygonal Mesh

Algorithm 1 Reconstruction and Validation of a Polygonal Mesh

```
1: function RECONSTRUCTMESH(pointCloud, maxIterationsVertices, maxIterationsFaces)
       iterationVertices \leftarrow 0
       while iterationVertices < maxIterationsVertices do
 3:
          vertices \leftarrow GENERATEVERTICESFROMPOINTCLOUD(pointCloud)
 4:
          if not have_stop_token(vertices) then
 5:
              iterationVertices \leftarrow iterationVertices + 1
              continue
 7:
 8:
          iterationFaces \leftarrow 0
          while iterationFaces < maxIterationsFaces do
 9:
              faces \leftarrow GENERATEFACESFROMVERTICES(vertices)
10:
              if not have_stop_token(faces) then
11:
                 iterationFaces \leftarrow iterationFaces + 1
12:
                 continue
13:
              if not is_floor_covering_pointcloudxy(faces) then
14:
15:
                 if ARE_MISSING_FLOOR_VERTICES(faces) then
                     break
16:
                 else if ARE\_MISSING\_FLOOR\_FACES(faces) then
17:
                     iterationFaces \leftarrow iterationFaces + 1
18:
                     continue
19:
20:
              if not are_floor_edges_connected_to_walls(faces) then
                 iterationFaces \leftarrow iterationFaces + 1
21:
22:
                 continue
              if are_diagonal_edges_present_on_walls(faces) then
23:
                 iterationFaces \leftarrow iterationFaces + 1
24:
                 continue
25:
              cadModel \leftarrow BUILDCADMODEL(vertices, faces)
26:
27:
              return cadModel
28:
          iterationVertices \leftarrow iterationVertices + 1
       raise "Maximum number of iterations has been reached"
29:
```